Numerical prediction of railhead rolling contact fatigue crack growth

Wear 530–531 (2023) 205003

Contents lists available at ScienceDirect

Wear

journal homepage: www.elsevier.com/locate/wear

Numerical prediction of railhead rolling contact fatigue crack growth

Mohammad Salahi Nezhad [a,*], Fredrik Larsson [a], Elena Kabo [b], Anders Ekberg [b]

[a] CHARMEC/Department of Industrial and Materials Science, Chalmers University of Technology, SE-412 96 Gothenburg, Sweden
[b] CHARMEC/Department of Mechanics and Maritime Sciences, Chalmers University of Technology, SE-412 96 Gothenburg, Sweden

ARTICLE INFO

Keywords:
Rolling contact fatigue
Crack growth direction
Crack face friction
Vector crack tip displacement
Crack growth rate

ABSTRACT

The influence of crack face friction on predicted crack growth in a 2D rail model is investigated numerically. An isolated surface-breaking inclined rolling contact fatigue crack is propagated into a rail under (i) a moving contact load, (ii) a combined thermal and contact load, and (iii) a combination of (rail) bending and contact load. Crack face friction is modelled by the Coulomb friction model. The crack growth direction is predicted using an accumulated vector crack tip displacement criterion and two Paris-type equations are employed to estimate crack growth rates. The model is validated towards a twin-disc experiment in the literature. The influence of the crack face friction coefficient and parameters in the crack growth direction criterion are assessed. Frictional cracks tend to go deeper into the rail although the influence under combined thermal and contact loading is minor. In all investigated load scenarios, crack face friction is shown to reduce crack growth rates.

1. Introduction

Managing Rolling Contact Fatigue (RCF) cracks is an inevitable and expensive part of the maintenance of railway tracks with potential safety-related consequences [1]. Cost and risk magnitudes are largely governed by the depth of crack propagation – shallow cracks result in limited material fall-out, and require moderate surface reprofiling through grinding or milling, whereas deeper cracks cause deeper material fall-out or transverse fracture, which requires heavy reprofiling or rail replacement. The main motivation for the current study is to be able to predict how operational conditions influence the propensity for deeper and transverse growth. Since the ability for tests is limited due to scaling issues and the requirements for complex and timely tests, this requires the development of a reliable numerical framework and predictive models. In previous studies [2,3] such a predictive framework has been developed and verified towards biaxial fatigue crack growth tests and twin-disc tests featuring RCF crack growth. The framework has been employed to investigate the influence of the operational loads on the RCF crack path for a frictionless crack [4]. The current study aims at improving the predictive model by accounting for crack face friction as well as estimating crack growth rates.

In the context of RCF of wheels and rails, crack face friction is affected by the penetration of lubrication (e.g., water or grease) into the RCF cracks. This will lubricate crack faces and thereby decrease crack face friction. In addition, lubrication trapped in the crack may distribute pressure deeper into the crack and induce local pressurisation of the crack [5]. The effect of crack face friction on the shear loading of a crack subjected to rolling contact has been found to be significant [6]. Also, the combined influence of decreased friction and pressurisation on the crack loading has been extensively investigated [7–9]. In short, pressurisation of the crack will tend to open the crack (mode I), which prevents crack face contact. In the case of a closed crack, decreased friction will facilitate the sliding of the crack faces (modes II and III).

It has been shown in field tests [10] that water is indeed prone to penetrate surface initiated RCF cracks. However, for pressurisation to occur, the crack (or parts of it) also has to be fully sealed during the rolling contact in order to maintain the pressure. In a real wheel–rail contact where the cracking more relates to a network, see e.g. [11], this may be hard to achieve. Also, any pressurisation is likely confined to some parts of the cracks, and systematic analysis of this effect is challenging. For this reason, the current study focuses solely on the influence of crack face friction. Further, the study leaves the influence of different load scenarios on the crack loading, i.e. evolution of Stress Intensity Factors (SIFs), and focuses solely on the direction of crack propagation and estimation of relative crack growth rates under varying loading conditions.

Experimental assessment of the frictional behaviour at crack faces in contact is inherently difficult, and the conditions in the field are even more difficult to measure. Therefore, the most basic Coulomb model, characterised by a single coefficient of friction, is adopted in this study to quantify the effect of friction.

Crack growth rate is usually predicted by a growth law. The major challenge in this study is to account for the mixed-mode loading and

* Corresponding author.
E-mail address: salahi@chalmers.se (M. Salahi Nezhad).

https://doi.org/10.1016/j.wear.2023.205003
Received 27 February 2023; Received in revised form 9 May 2023; Accepted 3 June 2023
Available online 3 June 2023

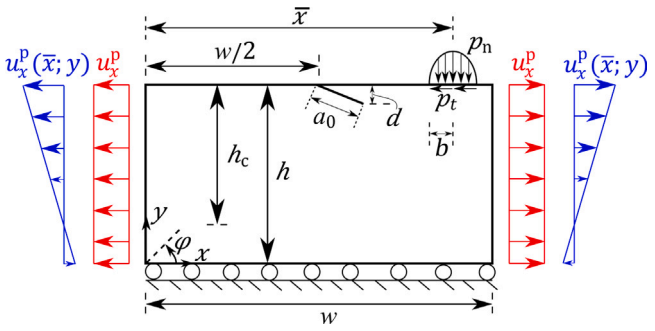

Fig. 1. A sketch of the 2D rail part with an inclined surface-breaking crack subjected to a Hertzian contact load (p_n, p_t) and constant longitudinal boundary displacements u_x^p (red), or boundary displacements $u_x^p(\bar{x};y)$ pertinent to rail bending (blue). The global Cartesian (x, y) coordinate system is indicated in the lower left corner. (For interpretation of the references to colour in this figure legend, the reader is referred to the web version of this article.)

crack path deviations, which alter the crack loading. To address this, it has for example been proposed in [12] to evaluate growth rates and directions using criteria based on material forces. Another widely used formulation for predicting crack growth rate is based on the Paris law [13]. Paris-type equations may employ different parameters as the driving force such as SIFs, e.g. [14], strain energy density factors, for instance [15], and cyclic J-integral (ΔJ), e.g. [16]. The SIF-based Paris-type equations usually use an equivalent SIF parameter under mixed-mode loading to account for mode interaction, see for instance [14,17,18].

Loading and deformation of propagating RCF cracks are in the current study evaluated using Finite Element (FE) simulations. Thereby, the study presents an extension of [4], where propagation of cracks under operational conditions was considered for the frictionless case. Motivated by the findings in [2,3], the direction of growth is predicted using an accumulative Vector Crack Tip Displacement (VCTD) criterion based on displacements extracted from linear elastic FE analyses. Two Paris-type equations are employed to estimate bounds for the crack growth rates. The qualitative influence of crack face friction on RCF crack growth is obtained by comparing predicted crack growth paths and rates for frictional and frictionless cracks.

2. Numerical framework

2.1. Model

Fig. 1 shows a rectangular (rail) section of width $w = 300$ mm and height $h = 100$ mm, which represents the rail domain in a 2D FE-model. The bottom side of the rail is restrained in the vertical direction ($u_y = 0$) and side edge displacements are prescribed in the horizontal direction ($u_x = u_x^p$).

A $d = 2$ mm deep surface-breaking inclined crack with a length of $a_0 = 4.3$ mm (initial inclination $\varphi_0 = -25°$ [19,20]), see Fig. 1, is modelled as a discrete crack. For crack face constraints in the normal and tangential directions, penalty formulations are employed in the FE-model. Coulomb friction is used in the constitutive equation where the tangential traction between two contacting surfaces, p_t, is evaluated as

$$\begin{cases} |p_t| \le \mu_{CF} p_n & v_t = 0 \quad \text{(stick condition)} \\ p_t = -\mu_{CF} p_n \frac{v_t}{|v_t|} & v_t \neq 0 \quad \text{(slip condition)} \end{cases}. \tag{1}$$

Here, v_t denotes the tangential (sliding) velocity, μ_{CF} and p_n are friction coefficient and normal contact pressure on the contacting surfaces, respectively. The employed FE-mesh is shown in Fig. 2 and consists of standard second-order quadrilateral (8-noded) elements with a size of 17 μm near the crack tip. The rail section is modelled as linearly elastic under plane strain conditions. The modulus of elasticity and the Poisson's ratio of the rail material are taken as $E_r = 210$ GPa and $\nu_r = 0.3$, respectively.

2.2. Load scenarios

Cyclic loading of the rail is considered, and the rail part is subjected to three different loads: wheel–rail contact load, rail bending load, and thermal load.

2.2.1. Contact load

The wheel–rail contact loads consist of contact pressure and frictional stresses. The wheel–rail contact is modelled using Hertzian theory. The 2D contact pressure, p_n, has an elliptic distribution along the contact surface, which for a given wheel load position, $\bar{x}$, is expressed as [21]

$$p_n(\bar{x};x) = \begin{cases} \frac{2P}{\pi b^2}\sqrt{b^2 - [x-\bar{x}]^2} & |x-\bar{x}| < b \\ 0 & |x-\bar{x}| \ge b \end{cases}, \tag{2}$$

where P is the 2D contact load magnitude (per unit thickness) and $|\bullet|$ represents the absolute value. For a given load magnitude, P, the semi-axis of the contact patch, b, is computed as

$$b = \sqrt{\frac{4PR}{\pi}\left(\frac{1-\nu_r^2}{E_r} + \frac{1-\nu_w^2}{E_w}\right)}. \tag{3}$$

Here, $R = 0.46$ m is the radius of the wheel and the elastic properties of the wheel material are taken as $E_w = 199$ GPa and $\nu_w = 0.3$.

It is presumed that frictional stresses in the wheel–rail interface follow the spatial distribution of the contact pressure (i.e. they are evaluated under an assumption of full slip) with a traction coefficient of f_{wr} which gives the frictional stresses as $p_t(\bar{x};x) = f_{wr}\, p_n(\bar{x};x)$. A wheel passage is simulated by moving the contact load along the top surface of the rail. During pure contact loading, the vertical edges of the rail are clamped in the global x–direction ($u_x^p = 0$), see Fig. 1.

2.2.2. Rail bending load

Rail bending occurs as a wheel traverses the rail. To evaluate the bending moment, a 6 m section of the track with a rail profile of 60E1 subjected to a passing wheel load of 7.5 t with a velocity of 100 km/h has been considered. The crack mouth is assumed to be positioned midspan in-between two adjacent sleepers, which corresponds to the centre of the considered track section. The evolution of the bending moment at the position of the crack mouth is computed by the in-house vertical dynamic vehicle–track interaction analysis code, DIFF [22]. The result is presented in Fig. 3, where the bending moment at the position of the crack mouth is evaluated for each position $\bar{x}$ of the load. The load position $\bar{x} = 0.15$ m corresponds to the situation that the load is at the position of the crack mouth. To quantify the magnitude of the boundary displacements of the 2D rail section due to the rail bending load, the rail section is modelled as an Euler–Bernoulli beam. Thus, the $u_x^p(\bar{x};y)$ is evaluated based on the moment–curvature relation for the presumed rail section using [23]

$$u_x^p(\bar{x};y) = \frac{M(\bar{x})\left[y - \left[h - h_c\right]\right] w}{2E_r I_z}, \tag{4}$$

where $M(\bar{x})$ is the bending moment at the wheel load position, $\bar{x}$, evaluated from Fig. 3, w is the length of the rail section, $h_c = 0.091$ m and $I_z = 30.5 \times 10^{-6}$ m^4 are the distance from the top surface of the rail to the neutral axis, see Fig. 1, and the moment of inertia of the rail profile [24], respectively.

2.2.3. Thermal load

Thermal stresses in rail result from restricted thermal contractions due to ambient temperature variations ΔT from the stress-free temperature. These longitudinal stresses along the rail can be quantified using a linear thermoelasticity assumption. More precisely, approximating the rail as homogeneous and perfectly confined in the axial direction, the corresponding boundary displacements are [23]

$$u_x^p = -\alpha_r \Delta T \frac{w}{2}. \tag{5}$$

Here, $\alpha_r = 11.5 \times 10^{-6}$ [1/°C] is the coefficient of thermal expansion for the rail material and w is the length of the rail section.

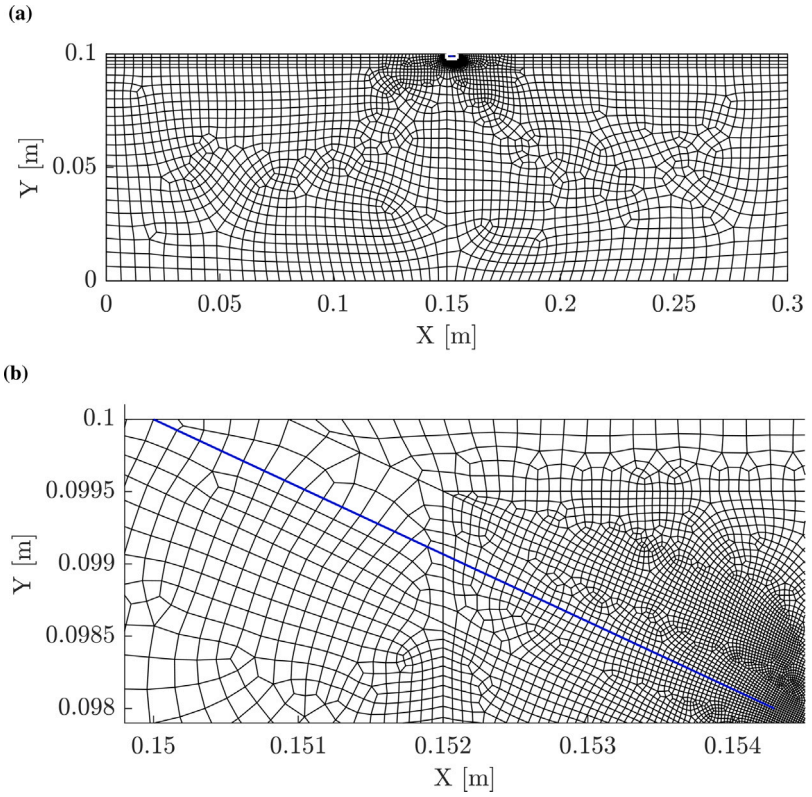

Fig. 2. The employed FE-mesh for the initial crack configuration. Thick blue lines show the crack. (a) Whole model. The crack area shown in (b) is marked with a white box. (b) Crack area. The smallest element size close to the crack tip is 17 μm.

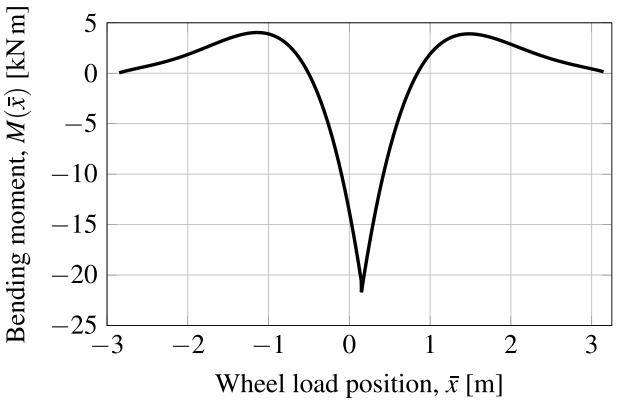

Fig. 3. Evolution of bending moment at the position of crack mouth as a function of the relative position of the wheel. Results from the dynamic vehicle–track simulation software DIFF [22].

2.3. Crack propagation

An (incrementally) stationary crack has been considered in this study, i.e. there is only propagation at the end of each load cycle. The crack growth direction and rate are predicted at the end of each load cycle using the accumulative VCTD criterion described in Section 2.3.1, and the procedure detailed in Section 2.3.2, respectively. The accumulated growth for multiple cycles is simulated by propagating the discrete crack in the predicted direction and repeating the process for each cycle. In this study, the incremental propagation of the crack is a pure discretisation parameter (rather than representing a certain number of load cycles). Hence, the crack path is predicted independent of the crack growth rate.

2.3.1. Crack growth direction criterion

The VCTD criterion proposed in [2] was developed based on the criterion suggested in [25] and modified to account for out-of-phase loading. It is utilised to predict crack growth direction for cyclic loading. Kinematic hardening effects are implicitly considered in the criterion, whereas effects from isotropic hardening are discarded since they are less pronounced for rail steel [26]. The criterion employs the relative crack face deformations in the normal and tangential directions, $\delta_{\mathrm{I}}(t)$ and $\delta_{\mathrm{II}}(t)$ respectively, as shown in Fig. 4b and postulates that the crack growth direction resulting from the presumed load cycle is in the direction of the crack driving displacement vector. A modified version of the VCTD criterion proposed in [2] is employed in this study, as briefly described below:

1. $\delta_{\mathrm{I}}(t)$ and $\delta_{\mathrm{II}}(t)$ are computed at each time instance t of the load cycle at a constant distance, d_{h}, from the crack tip, see Fig. 4. In this study, $d_{\mathrm{h}} \approx 52\,\mu\mathrm{m}$ was used.
2. To reflect kinematic hardening effects due to local plasticity at the crack tip, the 'amplitudes' of the crack face deformations, $\tilde{\delta}_{\mathrm{I/II}}(t)$, are employed. Using $\overline{\delta}_{\mathrm{I/II}} = \frac{1}{2}\left[\max_t\left(\delta_{\mathrm{I/II}}(t)\right) + \min_t\left(\delta_{\mathrm{I/II}}(t)\right)\right]$ as mid-values over the load cycle, 'amplitudes' of $\delta_{\mathrm{I}}(t)$ and $\delta_{\mathrm{II}}(t)$ are defined as

$$\tilde{\delta}_{\mathrm{I/II}}(t) = \delta_{\mathrm{I/II}}(t) - \overline{\delta}_{\mathrm{I/II}}. \tag{6}$$

3. Similar to [25], the instantaneous crack growth direction, $\vartheta(t)$, in the crack local coordinate system shown in Fig. 4a, and the instantaneous crack driving displacement, $\tilde{\delta}(t)$, are introduced as

$$\vartheta(t) = \arcsin\left(\frac{\tilde{\delta}_{\mathrm{II}}(t)}{\tilde{\delta}(t)}\right), \tag{7}$$

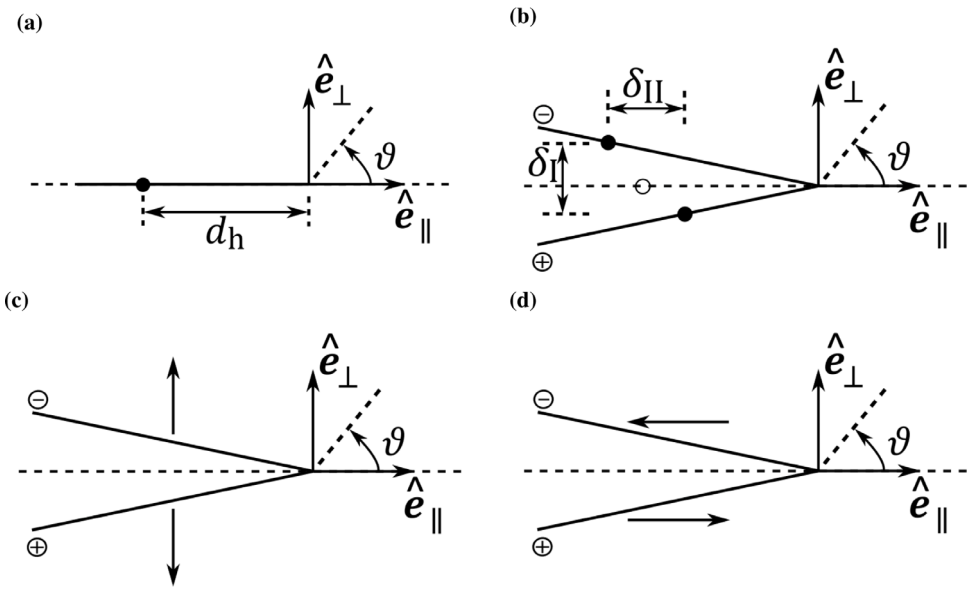

Fig. 4. Crack geometry configurations with local coordinate systems ($\hat{\mathbf{e}}_\parallel$, $\hat{\mathbf{e}}_\perp$). Dashed lines indicate the orientation of the undeformed crack. (a) Undeformed closed crack. (b) Crack face displacements. (c) Illustration of positive crack opening, δ_I. (d) Illustration of positive crack sliding, δ_{II}.

and[1]

$$\tilde{\delta}(t) = \sqrt{\langle\tilde{\delta}_I(t)\rangle^2 + 2\langle\tilde{\delta}_I(t)\rangle|\tilde{\delta}_{II}(t)| + 2\tilde{\delta}_{II}(t)^2}. \tag{8}$$

4. Finally, the crack propagation direction resulting from the full load cycle, ϕ, is defined by a unit vector in the crack tip local coordinate system, see Fig. 4a, as

$$\hat{\mathbf{e}}_\phi = \frac{\Delta\mathbf{a}}{\|\Delta\mathbf{a}\|}, \tag{9}$$

where $\Delta\mathbf{a}$ is the crack driving displacement vector and $\|\bullet\|$ indicates the Euclidean norm. The crack driving displacement vector is defined based on the 'rate-independent' response over the entire load cycle using

$$\Delta\mathbf{a} = \int_0^{T_c} \langle\frac{\mathrm{d}\tilde{\delta}(t)}{\mathrm{d}t}\rangle\hat{\mathbf{e}}_\vartheta(t)\,\mathrm{d}t. \tag{10}$$

Here, T_c denotes the duration of the load cycle and $\hat{\mathbf{e}}_\vartheta$ is the unit vector in the direction of the $\vartheta(t)$, evaluated from Eq. (7). In addition, the influence of the reversed shear deformations[2] can be accounted for in the evaluation of the crack driving displacement vector by utilising a reversed shear threshold parameter, ψ. Thereby, contributions to the integral in Eq. (10) can be omitted if the shear is acting in the reversed direction for (sufficiently) closed cracks. More detailed information in this regard was presented in [2,4]. The formulation in Eq. (10) implies neglecting the reversed shear condition.

2.3.2. Crack growth rate

The phase angle between the modes changes over time in the considered non-proportional loading. There are then two possible ways to evaluate the resulting crack growth rate for the entire load cycle: the accumulation of instantaneous contribution (similar to what is employed in Section 2.3.1 for the growth direction), or using classical growth laws. Having 2D plane strain models as well as considering the complexity of the accumulation scheme of the instantaneous contributions and lack of sufficiently large experimental data to calibrate the adopted scheme, the crack growth rate is in this study evaluated using growth laws available in the literature.

One of the most common baselines for predicting crack growth rate is Paris law [13]. It relates the crack growth rate, $\mathrm{d}a/\mathrm{d}N$, to the range of SIF, ΔK, with a power law, $\mathrm{d}a/\mathrm{d}N = C(\Delta K)^m$. In this equation, C and m are material parameters. In the following, these are taken the same in modes I and II[3]. To account for the non-proportionality of the loads, two Paris-type equations are employed in this study for rate predictions assuming different interactions between mode I and mode II loads. For a lower estimate, the loading of the modes is presumed to be sequentially applied and the total growth rate is the sum of the contributions of mode I and mode II [27], see Fig. 5a,

$$(\frac{da}{dN})_l = C(\Delta K_I)^m + C(\Delta K_{II})^m. \tag{11}$$

The second extreme is to consider the loading of the modes simultaneously applied. The driving force in Paris law, ΔK, is then evaluated based on energy considerations as $\Delta K_{eq.} = \sqrt{(\Delta K_I)^2 + (\Delta K_{II})^2}$ [18] whereby the upper estimate of the crack growth rate can then be evaluated as

$$(\frac{da}{dN})_u = C(\Delta K_{eq.})^m. \tag{12}$$

In this study, $C = 6.89\times10^{-9}\,\frac{\mathrm{mm/cycle}}{(\mathrm{MPa}\sqrt{\mathrm{m}})^m}$ and $m = 3$ is employed, which is pertinent to Ferritic-pearlitic steel in mode I loading with $R = \sigma_{min}/\sigma_{max} \approx 0$ [28].

Eqs. (11) and (12) require the calculation of SIFs. There are several methods in computational fracture mechanics to evaluate SIFs values such as utilising Green's function [29], the stress interpretation method, the displacement interpretation method, and from the J-integral, see e.g. [30]. One computationally efficient way is to use the displacement fields close to the crack tip for mixed-mode loading of mode I and mode II in an isotropic linear elastic material. In the crack tip local coordinate system shown in Fig. 4a, the displacement fields in the vicinity of the

[1] $\langle\bullet\rangle$ denotes the Macaulay brackets, $\langle\bullet\rangle = \frac{1}{2}[\bullet + |\bullet|]$.

[2] The reversed shear deformations are defined as shear deformations of the crack which are in the opposite direction to the assumed direction of crack growth, cf [4].

[3] Since the aim of the current study is to qualitatively compare the crack growth rates under different load scenarios, this assumption is utilised. For a case of quantitative rate prediction, the assumption causes some inaccuracies in the predicted rates.

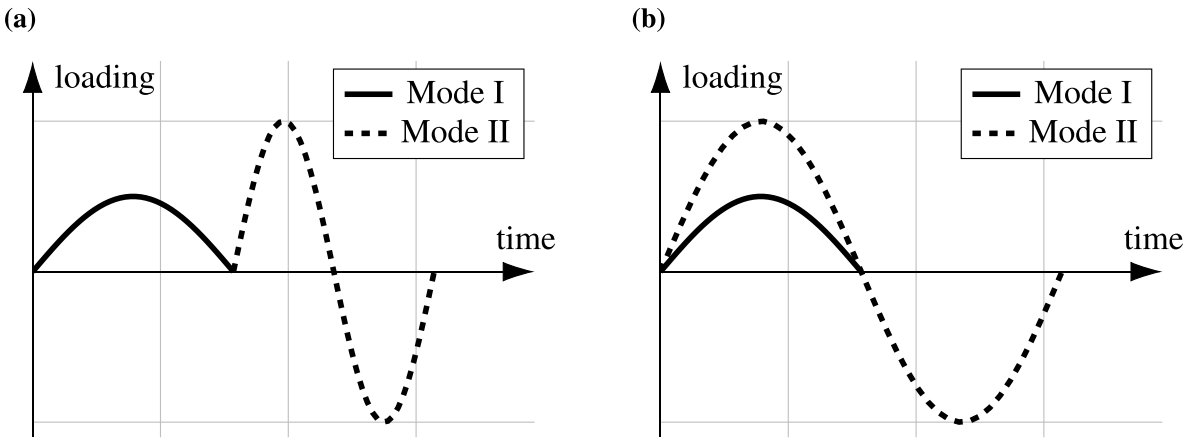

Fig. 5. An illustration of SIF evolutions for crack growth rate estimates under mixed-mode loading. (a) Lower estimate. (b) Upper estimate.

crack tip in time step t are expressed in terms of SIFs (K_{I} and K_{II}) as [30]

$$\begin{aligned} u_{\parallel}(r,\vartheta,t) &= \frac{K_{\mathrm{I}}(t)}{2\mu}\sqrt{\frac{r}{2\pi}}\cos\left(\frac{\vartheta}{2}\right)\left[\kappa-1+2\sin^2\left(\frac{\vartheta}{2}\right)\right] \\ &\quad+\frac{K_{\mathrm{II}}(t)}{2\mu}\sqrt{\frac{r}{2\pi}}\sin\left(\frac{\vartheta}{2}\right)\left[\kappa+1+2\cos^2\left(\frac{\vartheta}{2}\right)\right], \\ u_{\perp}(r,\vartheta,t) &= \frac{K_{\mathrm{I}}(t)}{2\mu}\sqrt{\frac{r}{2\pi}}\sin\left(\frac{\vartheta}{2}\right)\left[\kappa+1-2\cos^2\left(\frac{\vartheta}{2}\right)\right] \\ &\quad-\frac{K_{\mathrm{II}}(t)}{2\mu}\sqrt{\frac{r}{2\pi}}\cos\left(\frac{\vartheta}{2}\right)\left[\kappa-1-2\sin^2\left(\frac{\vartheta}{2}\right)\right], \end{aligned} \tag{13}$$

where r shows the radial distance from the crack tip, $\mu = \frac{E}{2(1+\nu)}$ is the shear modulus and $\kappa = 3-4\nu$ for plane strain conditions. In order to use the crack face displacements measured in Section 2.3.1 for evaluating SIFs, the top and bottom surface of the crack can be expressed as $(r,\vartheta,t)=(d_{\mathrm{h}},\pi,t)$ and $(r,\vartheta,t)=(d_{\mathrm{h}},-\pi,t)$, respectively. Using $\delta_{\mathrm{I}}(d_{\mathrm{h}},t) = u_{\perp}(d_{\mathrm{h}},\pi,t)-u_{\perp}(d_{\mathrm{h}},-\pi,t)$ and $\delta_{\mathrm{II}}(d_{\mathrm{h}},t) = u_{\parallel}(d_{\mathrm{h}},\pi,t)-u_{\parallel}(d_{\mathrm{h}},-\pi,t)$ gives the approximations

$$K_{\mathrm{I}}(d_{\mathrm{h}},t) = A(d_{\mathrm{h}})\delta_{\mathrm{I}}(t), \qquad K_{\mathrm{II}}(d_{\mathrm{h}},t) = A(d_{\mathrm{h}})\delta_{\mathrm{II}}(t), \tag{14}$$

where the scaling for varying distance d_{h} can be identified as

$$A(d_{\mathrm{h}}) = \frac{E}{8(1-\nu^2)}\sqrt{\frac{2\pi}{d_{\mathrm{h}}}}. \tag{15}$$

This shows that SIFs can be evaluated directly from the crack face displacements if a sufficiently dense mesh is employed in the vicinity of the crack tip. The ranges of SIFs over a load cycle can then be computed using

$$\begin{aligned} \Delta K_{\mathrm{I}}(d_{\mathrm{h}}) &= \max_t\left(K_{\mathrm{I}}(d_{\mathrm{h}},t)\right)-\min_t\left(K_{\mathrm{I}}(d_{\mathrm{h}},t)\right), \\ \Delta K_{\mathrm{II}}(d_{\mathrm{h}}) &= \max_t\left(K_{\mathrm{II}}(d_{\mathrm{h}},t)\right)-\min_t\left(K_{\mathrm{II}}(d_{\mathrm{h}},t)\right). \end{aligned} \tag{16}$$

3. Analyses and results

The FE-model detailed in Section 2.1 subjected to the three different load scenarios of pure contact load, combined thermal and contact loads, and combined bending and contact loads, as described in Section 2.2, was implemented in ABAQUS/CAE [31]. The crack was propagated in an unbiased fashion in the predicted direction with a growth increment of 0.2 mm, as discussed in Section 2.3. The resolved displacement fields were post-processed in MATLAB [32] in order to evaluate the crack growth direction and rate at the end of the load cycle based on the accumulated VCTD criterion outlined in Section 2.3.1 and the procedure described in Section 2.3.2, respectively. Crack paths presented in the following subsections were evaluated during three growth increments, unless otherwise stated. The crack growth rate was also predicted to qualitatively compare the influence of the considered load scenarios on the crack growth rate.

3.1. Validation towards twin-disc experiment

The numerical predictions were compared against a twin-disc experiment described in [33]. In the considered experiment (designated as 'GO' in [33]), 500 unlubricated cycles were initially applied to initiate damage in the specimen and then 30 554 cycles with 'graphite in mineral oil' as the lubricant between wheel and rail discs were considered. The maximum Hertzian contact pressure and the traction coefficient in the lubricated phase were measured as $p_{\max} = 1500$ MPa and $f_{\mathrm{wr}} = 0.04$, respectively. After the test, a crack with a depth of 280 μm and approximately 900 μm long was found. The crack path and the average crack growth rate, i.e. the total length of the crack divided by the total number of lubricated cycles, are shown in Fig. 6 (labelled as 'experiment').

A rectangular part of the rail disc with width $w = 20$ mm and height $h = 10$ mm, which has a frictionless surface-breaking crack of length $a_0 = 450$ μm in the direction of $\varphi_0 \approx -18°$, was simulated under plane strain conditions and loaded by a contact load with $f_{\mathrm{wr}} = 0.04$, see Fig. 1. The employed FE-mesh consists of standard second-order quadrilateral (8-noded) elements with a size of 11 μm near the crack tip. Using contact formulae in [23] considering the maximum Hertzian contact pressure employed in the test gives the magnitude of contact load and the contact patch as $P \approx 0.72$ MN/m and $b \approx 0.3$ mm, respectively.

The predicted crack path considering the reversed shear condition in the VCTD criterion (cf. [4]) with the reversed shear threshold parameter $\psi = 0.01$ and growth rates for two growth increments are shown in Fig. 6 (named as '$\psi = 0.01$'). The predicted crack path does not capture the experimental path. This can be due to employing the reversed shear condition in the growth direction criterion since reversed shear instances, in this case, can promote crack growth in the negative direction of the crack tip local coordinate system, see Fig. 4a. To investigate this, the reversed shear condition is removed from the growth direction criterion, i.e. following the formulation detailed in Section 2.3.1, and the predicted crack path and the growth rate are presented in Fig. 6 (labelled as 'w/o ψ'). The predicted crack path is now following the observed path in the experiment better. The average crack growth rate in the experiment may not be fully representative of the comparison of the predicted crack growth rates against the experiment due to estimations regarding material parameters, etc. Nevertheless, the order of the predicted crack growth rates is considered reasonable.

3.2. Load scenario – Pure contact load

A pure contact load magnitude of $P = 33.8$ MN/m with a traction coefficient of $f_{\mathrm{wr}} = 0.3$ was applied to the FE-model shown in Fig. 1 with $u_x^{\mathrm{p}} = 0$. According to Eq. (3), the semi-axis of the contact patch was $b = 13.3$ mm.

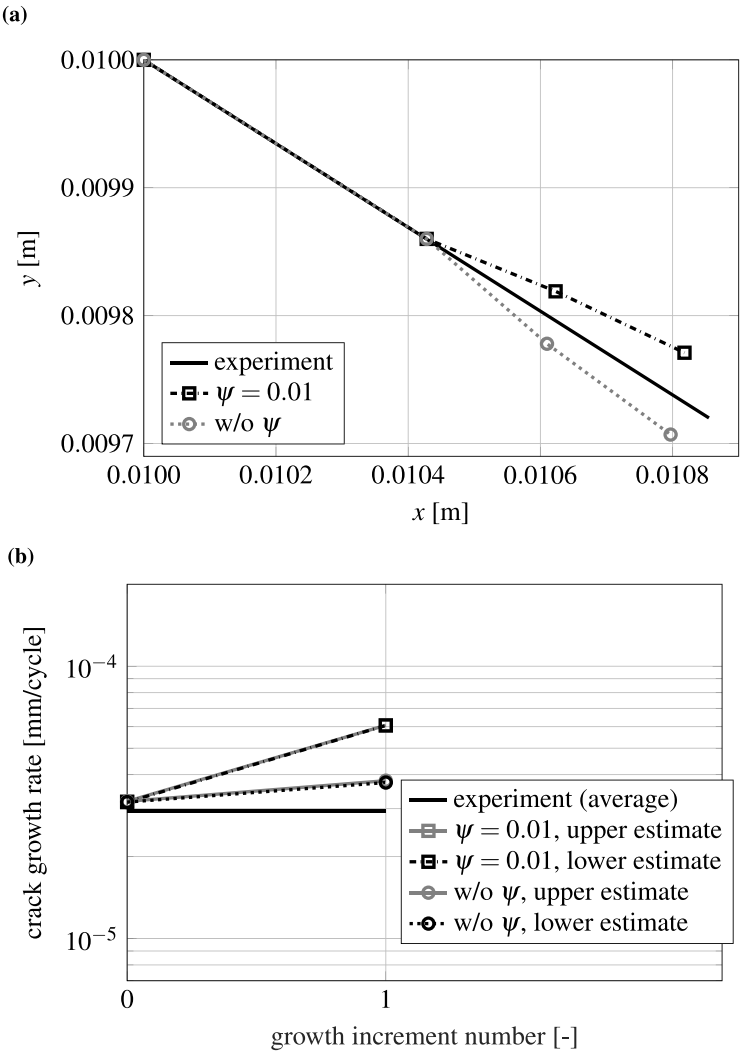

Fig. 6. Comparison of the predicted crack growth for a twin-disc experiment with a frictionless crack ($\mu_{CF} = 0$) and experimental results [33] under pure contact load with $P \approx 0.72$ MN/m and $f_{wr} = 0.04$. (a) Crack paths. (b) Crack growth rates.

In order to investigate the influence of the crack face friction on the crack growth direction, the predicted crack paths for a crack with a crack face friction coefficient of $\mu_{CF} = 0$, $\mu_{CF} = 0.3$ and $\mu_{CF} = 0.5$ are presented in Fig. 7. The crack growth directions were here evaluated considering the reversed shear condition in the growth direction criterion, as proposed in [4], with a reversed shear threshold parameter $\psi = 0.01$. It is expected that crack face friction truncates the crack shear deformations. This means a crack with higher crack face friction should have a higher share of mode I loading, and should grow into the rail with less deviation from the initial crack, i.e. more towards mode I growth, in comparison to the frictionless crack. Fig. 7 reflects this expectation.

Neglecting the reversed shear condition in the growth direction criterion, similar to Section 3.1, can be considered for the results presented in Fig. 7. This gives the predicted crack paths and rates shown in Fig. 8. The trend of the predicted crack paths is almost similar to the results in Fig. 7 with cracks growing deeper into the rail with increased friction and minor differences between crack paths for frictional cracks with $\mu_{CF} = 0.3$ and $\mu_{CF} = 0.5$. As shown in Fig. 8b, crack face friction reduces the growth rate of the crack by truncating the crack shear deformations and decreasing its loading. In addition, the higher share of mode I with increased friction leads to more distinction between lower and upper estimates of crack growth rate.

A mesh sensitivity analysis with three different mesh sizes was performed to study the effect of FE-discretisation on crack growth predictions. The predicted crack paths and growth rates using 'normal mesh' (as described in Section 2.1) with 64 262 Degrees Of Freedom (DOFs) (element size down to 17 μm near the crack tip) are then compared against predictions featuring a 'coarse mesh' with 42 500 DOFs (element size down to 22 μm near the crack tip) and a 'fine mesh' with 146 372 DOFs (element size down to 11 μm near the crack tip) in Figs. 9 and 10, respectively. The same d_h value was employed for all the studied FE-meshes. It is seen that the predictions are almost identical and it is concluded that the 'normal mesh' is sufficiently fine to be used in the analyses in this research.

3.3. Load scenario – Combined thermal and contact load

Boundary displacements, u_x^p, corresponding to $\Delta T = -20$ °C from Eq. (5) were applied to the model depicted in Fig. 1 in combination with contact loads $P = 7.3$ MN/m and $P = 33.8$ MN/m with $f_{wr} = 0.3$. The crack face friction coefficient was set to $\mu_{CF} = 0.3$.

Fig. 11a demonstrates the predicted crack paths for these load combinations considering the reversed shear condition in the crack growth direction criterion (cf. [4]) with the reversed shear threshold parameter $\psi = 0.01$. It is seen that the crack subjected to a combined

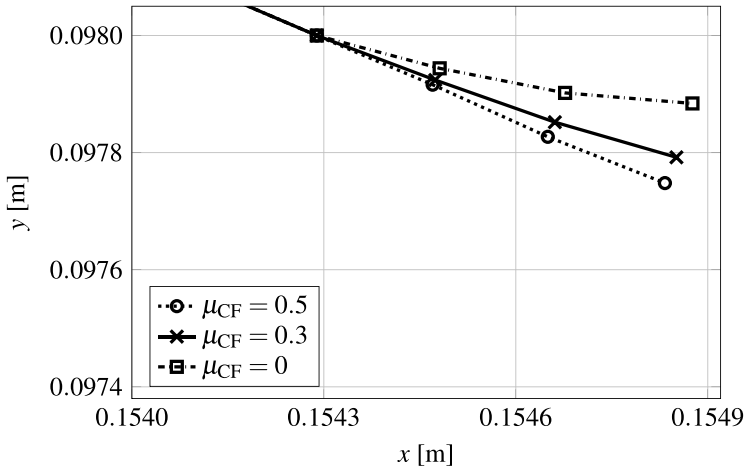

Fig. 7. Predicted crack paths for frictional crack with $\mu_{CF} = 0.3$ and $\mu_{CF} = 0.5$ and frictionless crack ($\mu_{CF} = 0$) under pure contact load with $P = 33.8\,\text{MN/m}$, $f_{wr} = 0.3$ and $\psi = 0.01$.

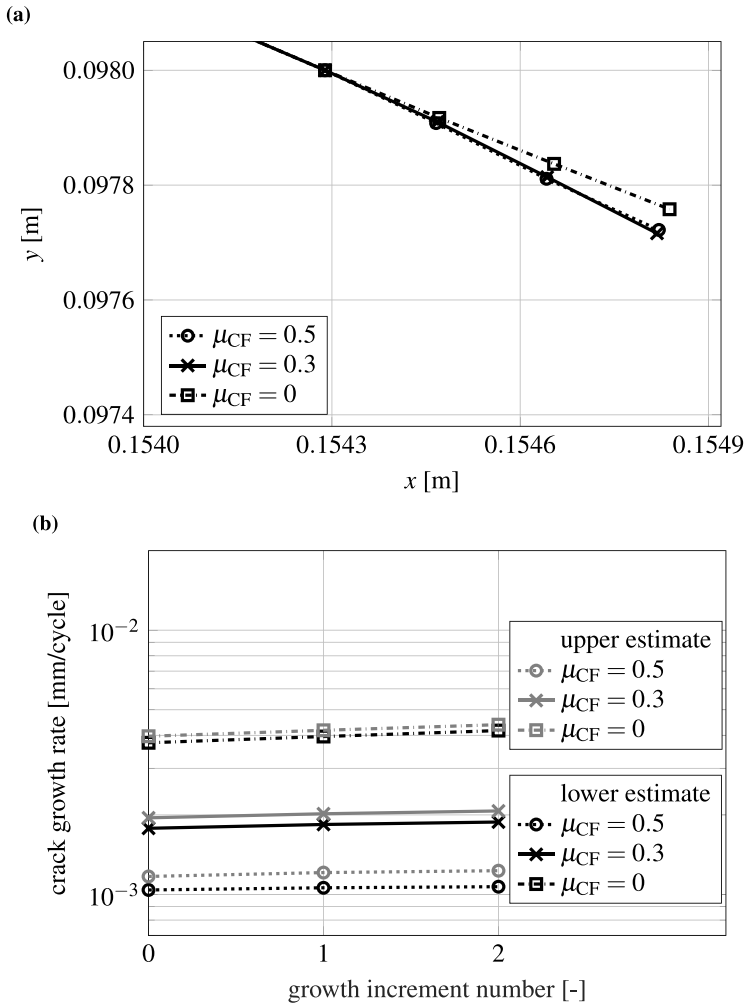

Fig. 8. Predicted crack growth for frictional crack with $\mu_{CF} = 0.3$ and $\mu_{CF} = 0.5$ and frictionless crack ($\mu_{CF} = 0$) under pure contact load with $P = 33.8\,\text{MN/m}$, $f_{wr} = 0.3$ and neglecting the reversed shear condition. (a) Crack paths. (b) Crack growth rates.

loading of thermal and 7.3 MN/m contact load tends to grow shallower than under pure contact load. This is not in line with the observations for a frictionless crack in [4], where gradual changes in the crack path from pure thermal to pure contact load were predicted. There are two possible reasons for this behaviour. It can be the influence of the mid-value ($\bar{\delta}$) correction (explained below), and/or an influence of the reversed shear condition employed in the growth direction criterion.

In operations, the length of the temperature load cycle, being on the order of hours or days, is much longer than the contact load cycle, which is on the order of milliseconds. Thus, several contact load cycles

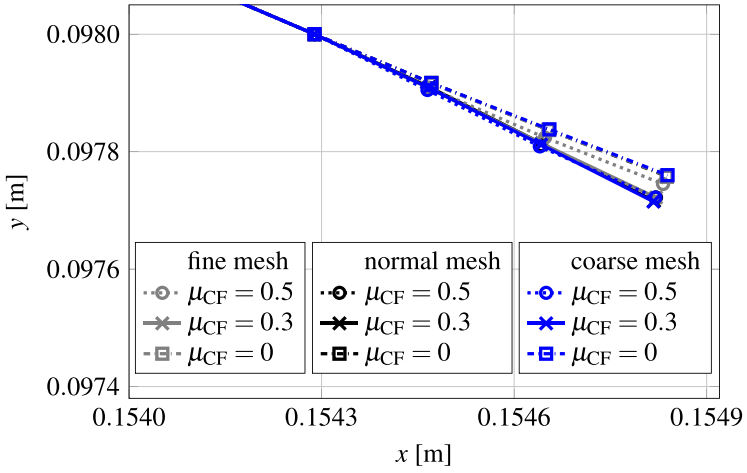

Fig. 9. Predicted crack paths for three different FE-meshes for frictional crack with $\mu_{CF} = 0.3$ and $\mu_{CF} = 0.5$ and frictionless crack ($\mu_{CF} = 0$) under pure contact load with $P = 33.8\,\text{MN/m}$, $f_{wr} = 0.3$ and neglecting the reversed shear condition.

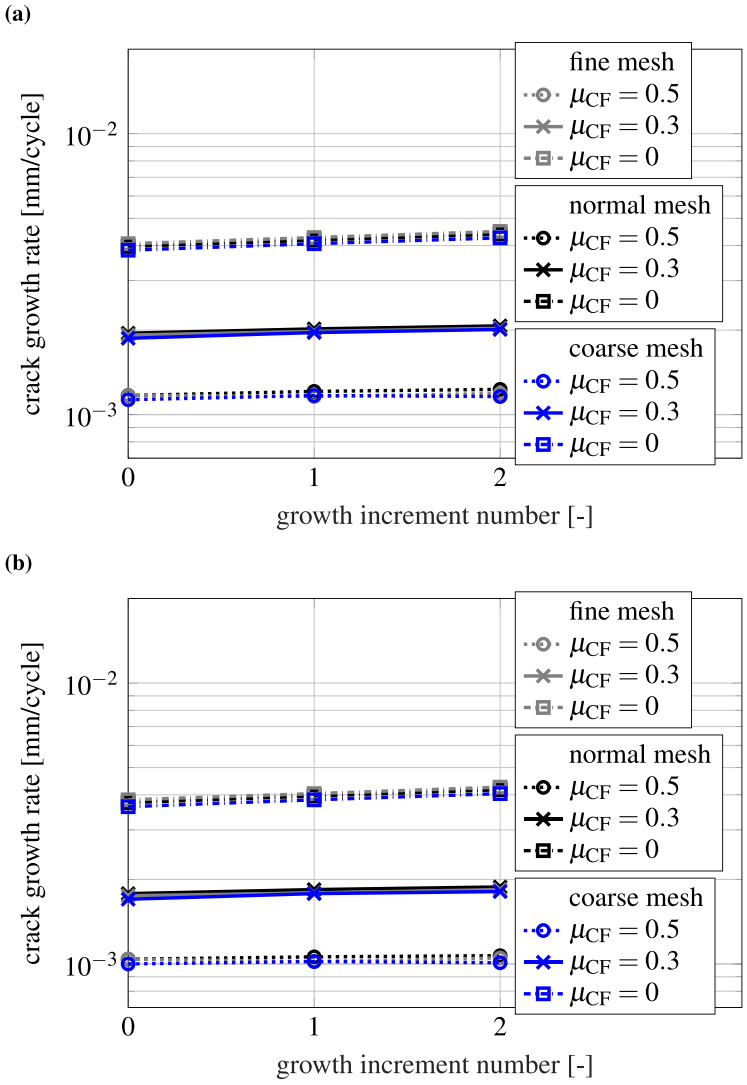

Fig. 10. Predicted crack growth rate for three different FE-meshes for frictional crack with $\mu_{CF} = 0.3$ and $\mu_{CF} = 0.5$ and frictionless crack ($\mu_{CF} = 0$) under pure contact load with $P = 33.8\,\text{MN/m}$, $f_{wr} = 0.3$ and neglecting the reversed shear condition. (a) Upper estimates. (b) Lower estimates.

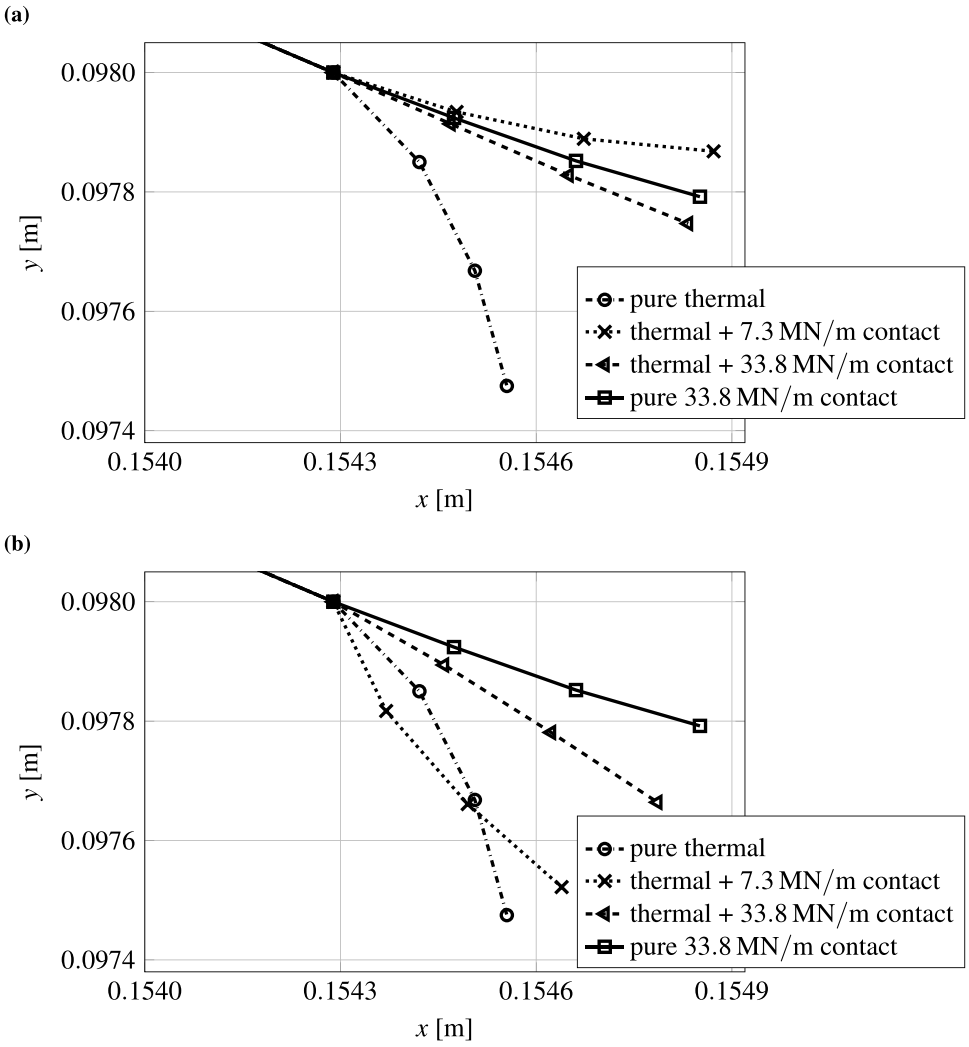

Fig. 11. Predicted crack paths for a frictional crack with $\mu_{CF} = 0.3$ under combined tensile thermal and contact loads with $f_{wr} = 0.3$ for $\psi = 0.01$. (a) Without $\bar{\delta}$-correction. (b) Considering $\bar{\delta}$-correction.

can occur within a certain temperature load cycle and the kinematic hardening effects at the crack tip thus mainly pertain to the contact load part for each load cycle. To consider this effect in the simulations, $\bar{\delta}$ is calculated based solely on the pure contact load part (henceforth denoted $\bar{\delta}$-correction). The pertinent results are presented in Fig. 11b. The predicted crack path for thermal and 7.3 MN/m contact load using $\bar{\delta}$-correction shows an expected behaviour based on the results from the frictionless crack in the last growth increment, cf. [4]. However, the crack under this load combination initially tends to grow deeper than for pure thermal load and has a 'jagged' path. This behaviour can be the influence of truncating contributions of the reversed shear instances since these should promote a shallower growth in general, and in particular in the first growth increment.

Figs. 12 and 13 show the predicted crack paths and growth rates, respectively, when neglecting the reversed shear condition in the growth direction criterion and considering the $\bar{\delta}$-correction. Comparing Fig. 11b and frictional paths in Fig. 12, it is seen that the 'jagged' path observed in Fig. 11b for the thermal and 7.3 MN/m contact load is eliminated.

Regarding the influence of the crack face friction on the predicted crack path, the trend of the results in Fig. 12 is the same for the frictional and frictionless paths with a little more deviation towards transverse growth for the thermal and 7.3 MN/m contact load in the case of a frictionless crack. This can be reasonable due to the fact that the frictionless crack should deviate more towards the shearing mode (mode II) as a result of having higher shear loading. Based on Fig. 12, it is concluded that the crack face friction has a moderate influence on the predicted crack path for combined thermal and contact loads.

Fig. 13 shows that the crack growth rate for the pure thermal load is much lower than the combined loads and pure contact load. This highlights the large influence of contact load on the crack growth rate due to the shallow crack. Moreover, it is observed that the crack growth rate for a case of thermal and 7.3 MN/m contact load is higher than for the pure thermal loading, and that the combination of thermal and 33.8 MN/m contact load has higher growth rate than a pure 33.8 MN/m contact load. This is to be expected as a reflection of the increased loading. Regarding the influence of crack face friction, it is seen that the crack face friction reduces the crack growth rate. These trends are consistent for lower and upper estimates.

To investigate crack growth predictions under a combination of compressive thermal and contact loads, the contact loads described earlier in this section were applied to the model shown in Fig. 1 in combination with boundary displacements, u_x^p, corresponding to $\Delta T = 20\,^{\circ}\mathrm{C}$ from Eq. (5).

The predicted crack paths when neglecting the reversed shear condition in the growth direction criterion and considering the $\bar{\delta}$-correction are presented in Fig. 14. It can be seen that the crack under pure compressive thermal load kinks upwards and has a 'jagged' path due to the crack opening occurring in the kinked branch of the crack after the first growth increment. For the combined loads, the crack paths

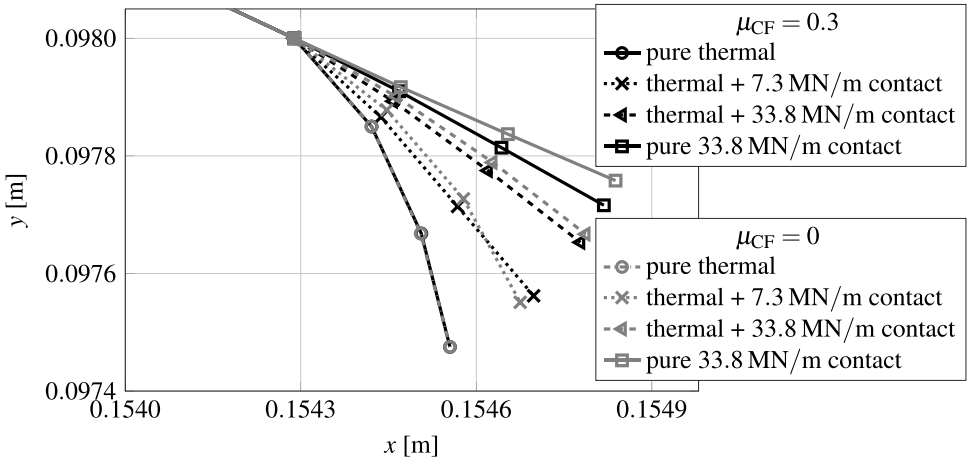

Fig. 12. Comparison of predicted crack paths under combined tensile thermal and contact loads with $f_{wr} = 0.3$ for frictional ($\mu_{CF} = 0.3$) and frictionless crack faces, neglecting the reversed shear condition and employing $\bar{\delta}$-correction.

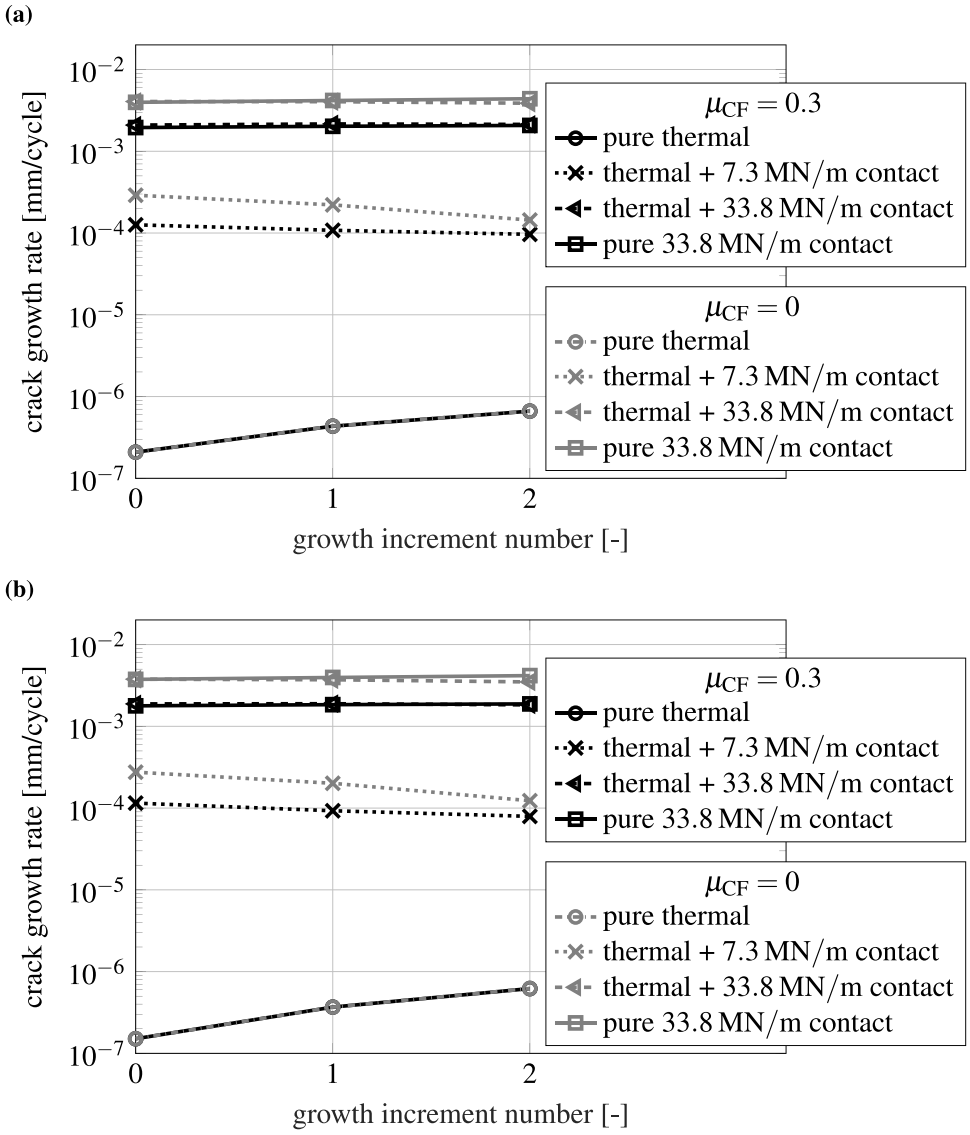

Fig. 13. Comparison of predicted crack growth rates under combined tensile thermal and contact loads with $f_{wr} = 0.3$ for frictional ($\mu_{CF} = 0.3$) and frictionless crack faces, neglecting the reversed shear condition and employing $\bar{\delta}$-correction. (a) Upper estimates. (b) Lower estimates.

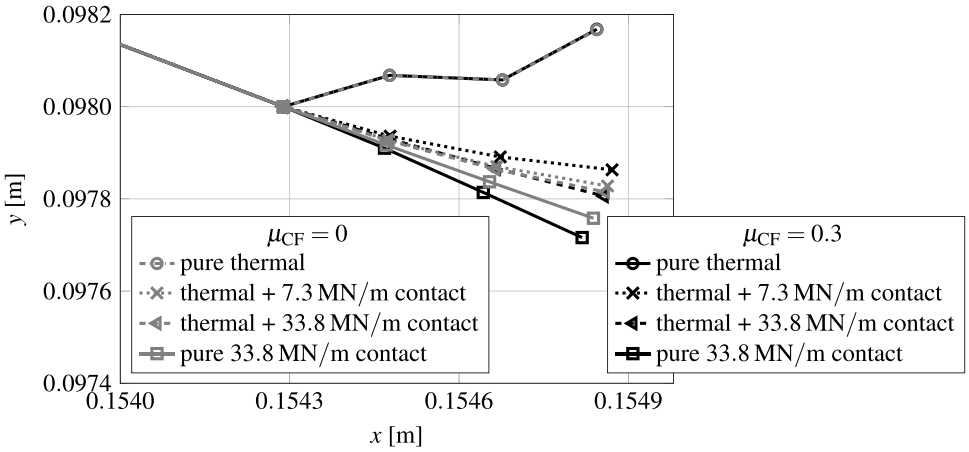

Fig. 14. Comparison of predicted crack paths under combined compressive thermal and contact loads with $f_{wr} = 0.3$ for frictional ($\mu_{CF} = 0.3$) and frictionless crack faces, neglecting the reversed shear condition and employing $\bar{\delta}$-correction.

are shallower than the pure contact path as a result of additional shear loading from the thermal load. Similar to the results in Fig. 12, a gradual change between the pure load cases is also observed in the predicted crack paths under combined loads while the paths here are closer to the pure contact path. In addition, the predicted crack paths under combined loads for frictional and frictionless cracks are closer than the case with the tensile thermal load, but the crack face friction still has a moderate influence in this case. Fig. 15 shows similar observations regarding the crack growth rate with slightly lower values, especially for the pure compressive thermal load case.

3.4. Load scenario – Combinations of bending and contact load

The model illustrated in Fig. 1 was loaded by boundary displacements pertinent to the bending load described by $u_x^p(\bar{x}; y)$ in Eq. (4). In addition, Hertzian contact loads of three different magnitudes of $P = 7.3\,\text{MN/m}$, $P = 14.0\,\text{MN/m}$ and $P = 33.8\,\text{MN/m}$ were applied. The traction and crack face friction coefficients were taken as $f_{wr} = 0.3$ and $\mu_{CF} = 0.3$, respectively.

The predicted crack paths under the combined loads are shown in Fig. 16 employing the reversed shear condition in the crack growth direction criterion (cf. [4]) with the reversed shear threshold parameter $\psi = 0.01$. The general trend of crack paths is close to predictions for frictionless cracks presented in [4] although two discrepancies are found. The combination of bending and 33.8 MN/m contact load results in a shallower path than the pure contact load, and the crack path for the combination of bending and 7.3 MN/m is slightly 'jagged' although the crack deviates less from the previous crack segment when it propagates, i.e. the share of the mode I in the crack loading is increasing.

The $\bar{\delta}$-correction, explained in Section 3.3, is not applicable to this load combination since the load cycle length of bending and contact are on the same order. Hence, what remains to investigate compared to the previous load scenarios is the influence of the reversed shear condition employed in the growth direction criterion. The predicted results when neglecting the reversed shear condition are presented in Figs. 17 and 18. The crack path predictions in Fig. 17 show a gradual change in predicted crack paths from the pure bending load to a pure contact load. Also, it is observed that the 'jagged' path for the combination of bending and 7.3 MN/m contact load is eliminated. In addition, Fig. 17 demonstrates that a crack with crack face friction is predicted to grow deeper into the rail than a frictionless crack.

Similar to the results in Section 3.3, Fig. 18 shows that the crack growth rate for the pure bending load is much lower compared to the combined loads and pure contact load. This shows the contact load has a large influence on the crack growth rate for the shallow crack. Furthermore, the crack could be expected to grow faster than under pure bending when it is subjected to combined loading due to the overall larger loads acting on the crack. However, for this load case, the combination of bending and 33.8 MN/m contact load results in a slower crack propagation than a pure contact load. This is due to the large compressive loading from bending that closes the crack as the contact load passes, see Fig. 3. Moreover, Fig. 18 demonstrates that the crack growth rate for a frictional crack is lower than a frictionless crack under combinations of bending and contact load due to the decreased shear deformation. These trends are consistent for upper and lower estimates.

4. Conclusions and outlook

A numerical procedure for simulating RCF crack growth under operational load scenarios while accounting for crack face friction has been developed. An isolated surface-breaking inclined crack is included in a 2D representation of the rail. The numerical model features linear elastic material under plane strain conditions and crack face friction is included using the Coulomb friction model. The crack growth direction has been evaluated from an accumulative VCTD criterion and two estimates for the crack growth rate have been computed based on the Paris law.

Comparing predictions of a twin-disc experiment against the experimental results and also results from simulations of combined contact load and bending or thermal loading identified the need to reconsider some of the adopted parameter values in the VCTD criterion. Neglecting the reversed shear condition led to a better match with the twin-disc experimental results. It was shown that frictional cracks under pure contact loading tend to grow deeper into the rail in comparison to frictionless cracks. By applying a $\bar{\delta}$-correction and neglecting the reversed shear condition previously employed in the criterion, a gradual transition in the predicted crack path from pure thermal to pure contact load conditions was observed as the contact load magnitudes were increased. For this load combination, friction had a moderate influence on predicted crack paths. Similar results were also achieved under combined compressive thermal and contact loads. A trend of gradual change between the pure load cases was also obtained for predicted crack paths under combinations of bending and contact load when the reversed shear condition was neglected. Similar to the case of a pure contact load, a frictional crack was predicted to propagate deeper into the rail. Regarding crack growth rates, it was concluded that crack face friction slows down the crack growth rate for all of the considered load cases by limiting the crack sliding.

The above conclusions were drawn based on a limited number of investigated loading scenarios. A full verification of 2D model predictions under operational loading scenarios is complex due to a scale difference

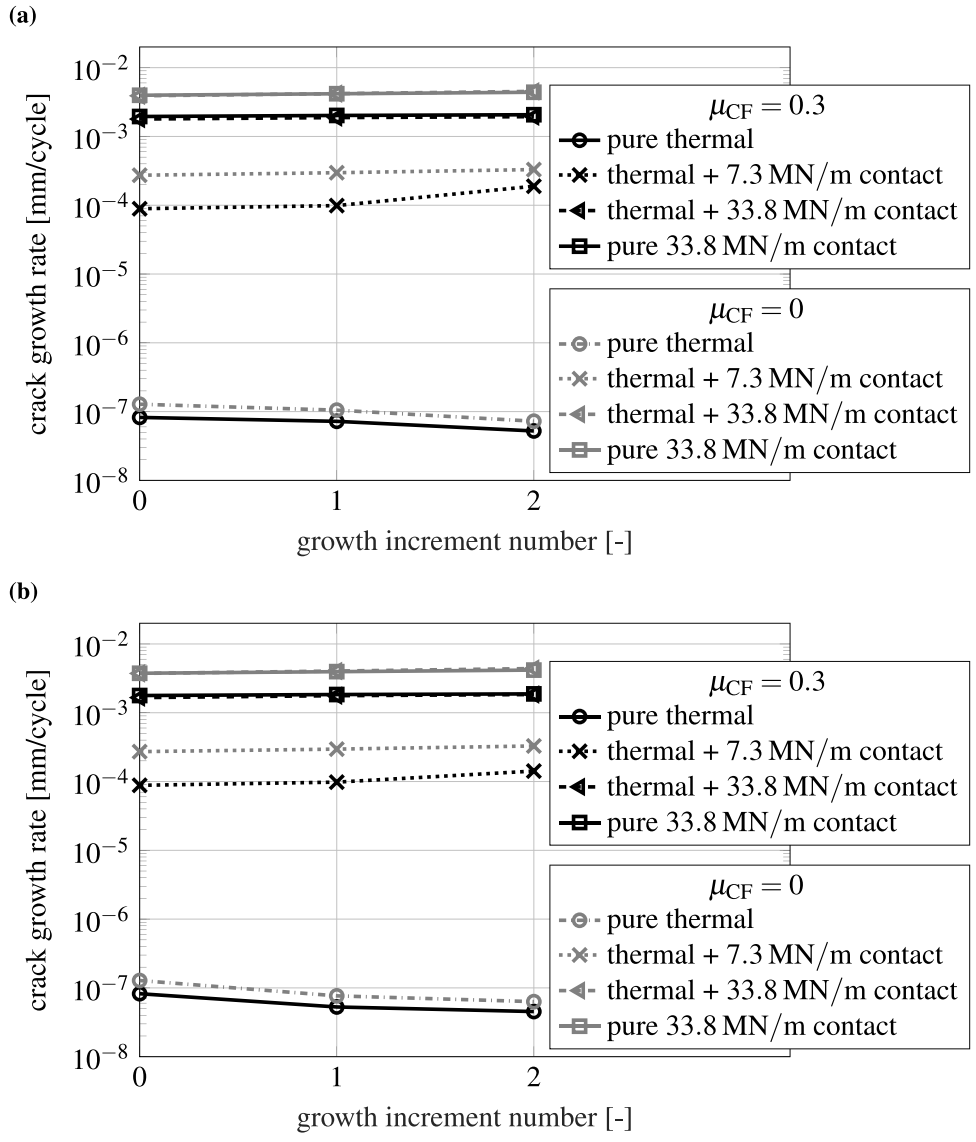

Fig. 15. Comparison of predicted crack growth rates under combined compressive thermal and contact loads with $f_{wr} = 0.3$ for frictional ($\mu_{CF} = 0.3$) and frictionless crack faces, neglecting the reversed shear condition and employing $\bar{\delta}$-correction. (a) Upper estimates. (b) Lower estimates.

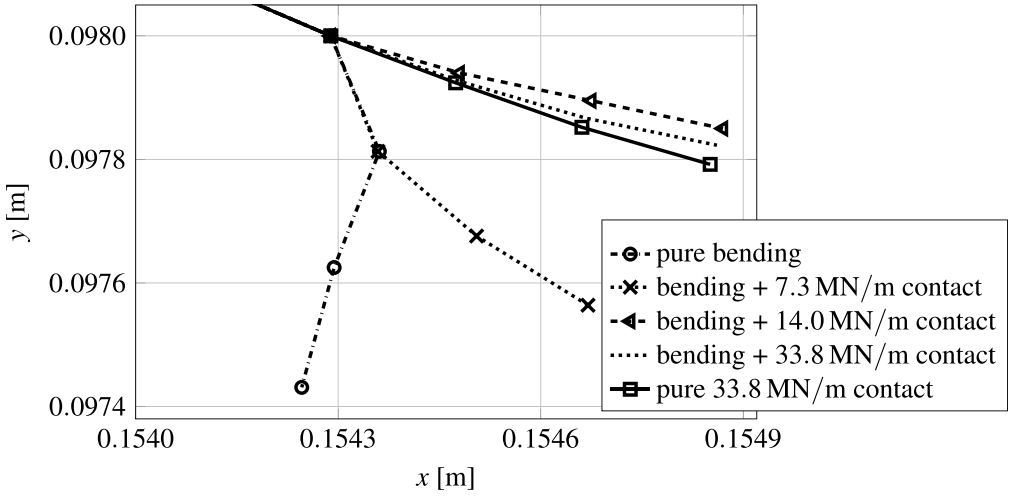

Fig. 16. Predicted crack paths for a crack with a friction coefficient of $\mu_{CF} = 0.3$ under combinations of bending and contact load with $f_{wr} = 0.3$ for $\psi = 0.01$.

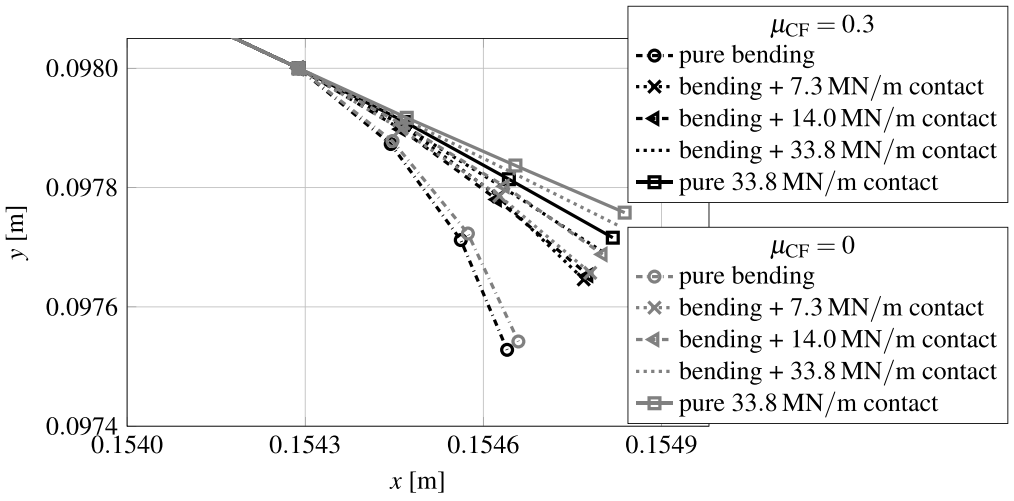

Fig. 17. Comparison of predicted crack paths for frictional ($\mu_{CF} = 0.3$) and frictionless crack faces under combinations of bending and contact load neglecting the reversed shear condition with $f_{wr} = 0.3$.

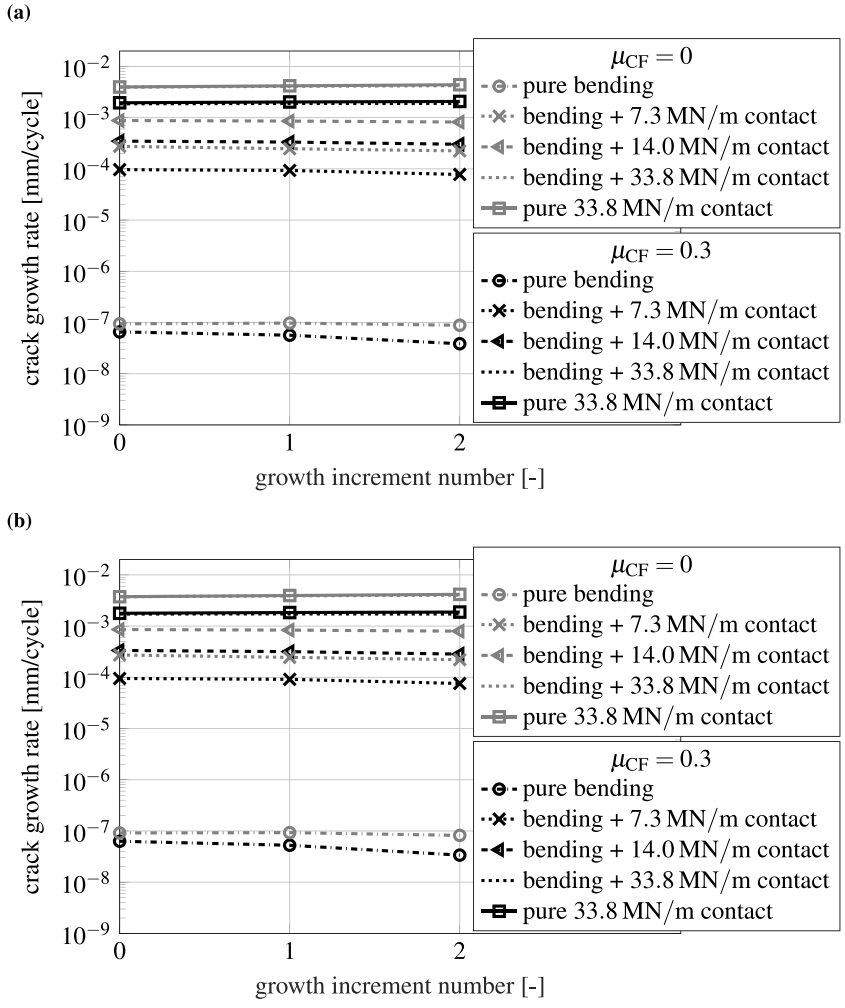

Fig. 18. Comparison of predicted crack growth rates for frictional ($\mu_{CF} = 0.3$) and frictionless crack faces under combinations of bending and contact load neglecting the reversed shear condition with $f_{wr} = 0.3$. (a) Upper estimates. (b) Lower estimates.

between the model (2D) and the measured data (3D). Verification towards field data for the combined loads has therefore so far not been considered in this research. The predictive model has however previously been validated towards controlled biaxial (tensile) tests [2] and in this study validated against a twin-disc test. In the extension, 3D modelling of the rail would allow for better quantitative verification. In the current study, it has been shown that the predicted crack path is sensitive to the employed values of parameters in the growth

direction criterion and the computational procedure: Good matches between simulations and four mixed-mode fatigue test experiments were reported by employing a reversed shear condition in the growth direction criterion in [2] while a better match was found for the twin-disc experiment simulation in this study by neglecting the reversed shear condition. Hence, special attention needs to be observed in the calibration of the model towards experimental results/field data.

CRediT authorship contribution statement

Mohammad Salahi Nezhad: Conceptualization, Methodology, Software, Validation, Writing – original draft, Writing – review & editing. **Fredrik Larsson:** Conceptualization, Methodology, Supervision, Resources, Writing – review & editing. **Elena Kabo:** Conceptualization, Methodology, Supervision, Resources, Writing – review & editing. **Anders Ekberg:** Conceptualization, Methodology, Supervision, Resources, Writing – review & editing.

Declaration of competing interest

The authors declare that they have no known competing financial interests or personal relationships that could have appeared to influence the work reported in this paper.

Data availability

Data will be made available on request.

Acknowledgements

The current study is part of the ongoing activities in CHARMEC – Chalmers Railway Mechanics (www.chalmers.se/charmec). Parts of the study have been funded from the European Union's Horizon 2020 research and innovation programme in the project In2Track3 under grant agreement No 101012456.

Funding

The work has been funded from CHARMEC, Sweden and from the European Union's Horizon 2020 research and innovation programme in the project In2Track3 under grant agreement No 101012456.

References

[1] E.E. Magel, Rolling Contact Fatigue: A Comprehensive Review, US Department of Transportation, Federal Railroad Administration, 2011, http://dx.doi.org/10.4224/23000318.

[2] D. Floros, A. Ekberg, F. Larsson, Evaluation of crack growth direction criteria on mixed-mode fatigue crack growth experiments, Int. J. Fatigue 129 (2019) 105075, http://dx.doi.org/10.1016/j.ijfatigue.2019.04.013.

[3] D. Floros, A. Ekberg, F. Larsson, Evaluation of mixed-mode crack growth direction criteria under rolling contact conditions, Wear 448-449 (2020) 203184, http://dx.doi.org/10.1016/j.wear.2020.203184.

[4] M. Salahi Nezhad, D. Floros, F. Larsson, E. Kabo, A. Ekberg, Numerical predictions of crack growth direction in a railhead under contact, bending and thermal loads, Eng. Fract. Mech. 261 (2022) 108218, http://dx.doi.org/10.1016/j.engfracmech.2021.108218.

[5] A.F. Bower, The influence of crack face friction and trapped fluid on surface initiated rolling contact fatigue cracks, J. Tribol. 110 (4) (1988) 704–711, http://dx.doi.org/10.1115/1.3261717.

[6] A.D. Hearle, K.L. Johnson, Mode II stress intensity factors for a crack parallel to the surface of an elastic half-space subjected to a moving point load, J. Mech. Phys. Solids 33 (1) (1985) 61–81, http://dx.doi.org/10.1016/0022-5096(85)90022-5.

[7] S. Bogdański, M. Olzak, J. Stupnicki, Numerical stress analysis of rail rolling contact fatigue cracks, Wear 191 (1) (1996) 14–24, http://dx.doi.org/10.1016/0043-1648(95)06685-3.

[8] S. Bogdański, M.W. Brown, Modelling the three-dimensional behaviour of shallow rolling contact fatigue cracks in rails, Wear 253 (1) (2002) 17–25, http://dx.doi.org/10.1016/S0043-1648(02)00078-9.

[9] S. Bogdański, P. Lewicki, M. Szymaniak, Experimental and theoretical investigation of the phenomenon of filling the RCF crack with liquid, Wear 258 (7) (2005) 1280–1287, http://dx.doi.org/10.1016/j.wear.2004.03.038.

[10] D.I. Fletcher, P. Hyde, A. Kapoor, Modelling and full-scale trials to investigate fluid pressurisation of rolling contact fatigue cracks, Wear 265 (9) (2008) 1317–1324, http://dx.doi.org/10.1016/j.wear.2008.02.025.

[11] K.A. Meyer, D. Gren, J. Ahlström, A. Ekberg, A method for in-field railhead crack detection using digital image correlation, Int. J. Rail Transp. 10 (6) (2022) 675–694, http://dx.doi.org/10.1080/23248378.2021.2021455.

[12] J. Brouzoulis, M. Ekh, Crack propagation in rails under rolling contact fatigue loading conditions based on material forces, Int. J. Fatigue 45 (2012) 98–105, http://dx.doi.org/10.1016/j.ijfatigue.2012.06.002.

[13] P. Paris, F. Erdogan, A critical analysis of crack propagation laws, J. Basic Eng. 85 (4) (1963) 528–533, http://dx.doi.org/10.1115/1.3656900.

[14] K. Tanaka, Fatigue crack propagation from a crack inclined to the cyclic tensile axis, Eng. Fract. Mech. 6 (3) (1974) 493–507, http://dx.doi.org/10.1016/0013-7944(74)90007-1.

[15] A.B. Patel, R.K. Pandey, Fatigue crack growth under mixed mode loading, Fatigue Fract. Eng. Mater. Struct. 4 (1) (1981) 65–77, http://dx.doi.org/10.1111/j.1460-2695.1981.tb01375.x.

[16] N.E. Dowling, J.A. Begley, Fatigue crack growth during gross plasticity and the J-integral, ASTM Special Tech. Publ. (1976) 82–103, http://dx.doi.org/10.1520/STP33940S.

[17] X. Yan, S. Du, Z. Zhang, Mixed-mode fatigue crack growth prediction in biaxially stretched sheets, Eng. Fract. Mech. 43 (3) (1992) 471–475, http://dx.doi.org/10.1016/0013-7944(92)90115-U.

[18] S. Bogdański, J. Stupnicki, M.W. Brown, D.F. Cannon, A two dimensional analysis of mixed-mode rolling contact fatigue crack growth in rails, Eur. Struct. Integr. Soc. 25 (1999) 235–248, http://dx.doi.org/10.1016/S1566-1369(99)80018-1.

[19] R. Heyder, G. Girsch, Testing of HSH® rails in high-speed tracks to minimise rail damage, Wear 258 (7) (2005) 1014–1021, http://dx.doi.org/10.1016/j.wear.2004.03.050.

[20] R. Stock, R. Pippan, RCF and wear in theory and practice—The influence of rail grade on wear and RCF, Wear 271 (1–2) (2011) 125–133, http://dx.doi.org/10.1016/j.wear.2010.10.015.

[21] K.L. Johnson, Contact Mechanics, Cambridge University Press, 1985, http://dx.doi.org/10.1017/CBO9781139171731.

[22] J.C.O. Nielsen, A. Igeland, Vertical dynamic interaction between train and track influence of wheel and track imperfections, J. Sound Vib. 187 (5) (1995) 825–839, http://dx.doi.org/10.1006/jsvi.1995.0566.

[23] S.P. Timoshenko, J.N. Goodier, Theory of Elasticity, McGraw-Hill, 1951.

[24] CEN. Railway applications. track. rail. vignole railway rails 46 kg/m and above. EN 13674-1:2011, European Committee for Standardization, 2011.

[25] C. Li, Vector CTD criterion applied to mixed mode fatigue crack growth, Fatigue Fract. Eng. Mater. Struct. 12 (1) (1989) 59–65, http://dx.doi.org/10.1111/j.1460-2695.1989.tb00508.x.

[26] K.A. Meyer, M. Ekh, J. Ahlström, Modeling of kinematic hardening at large biaxial deformations in pearlitic rail steel, Int. J. Solids Struct. 130–131 (2018) 122–132, http://dx.doi.org/10.1016/j.ijsolstr.2017.10.007.

[27] S.L. Wong, P.E. Bold, M.W. Brown, R.J. Allen, Fatigue crack growth rates under sequential mixed-mode I and II loading cycles, Fatigue Fract. Eng. Mater. Struct. 23 (8) (2000) 667–674, http://dx.doi.org/10.1046/j.1460-2695.2000.00342.x.

[28] N.E. Dowling, Mechanical Behavior of Materials: Engineering Methods for Deformation, Fracture, and Fatigue, Pearson Education, 2012.

[29] D.I. Fletcher, J.H. Beynon, A simple method of stress intensity factor calculation for inclined fluid-filled surface-breaking cracks under contact loading, Proc. Inst. Mech. Eng., Part J: J. Eng. Tribol. 213 (4) (1999) 299–304, http://dx.doi.org/10.1243/1350650991542686.

[30] M. Kuna, Finite Elements in Fracture Mechanics: Theory - Numerics - Applications, Springer Netherlands, 2013.

[31] ABAQUS/Standard User's Manual (Version 2020), Dassault Systèmes Simulia Corp., 2020.

[32] MATLAB 9.7.0.1190202 (Version R2019b), The MathWorks Inc., 2019.

[33] D.I. Fletcher, J.H. Beynon, The influence of lubricant type on rolling contact fatigue of pearlitic rail steel, Tribology Ser. 36 (1999) 299–310, http://dx.doi.org/10.1016/S0167-8922(99)80051-0.